When is curvature-level geoid validation feasible? A detectability-and-identifiability design rule, demonstrated on GSVS17

Russell David Moore

Highreach Institute for Scientific Exploration, Highreach Foundation LLC, Albany, NY, USA
contact@highreachfoundation.com
ORCID: 0000-0003-3939-3350

Peer review status

This is a non-peer-reviewed preprint submitted to EarthArXiv. It is intended for submission to the *Journal of Geodesy* for peer review. Subsequent peer-reviewed versions of this manuscript may differ from this version.

When is curvature-level geoid validation feasible? A detectability-and-identifiability design rule, demonstrated on GSVS17

Russell David Moore
Highreach Institute for Scientific Exploration, Highreach Foundation LLC, Albany, NY, USA
ORCID: 0000-0003-3939-3350 contact@highreachfoundation.com

June 21, 2026

Abstract

Geoid-model validation compares observed geoid heights and slopes against models; extending it by one differential order, to curvature, raises a design question: for what geometry, precision, and terrain is a curvature-level comparison decisive? In an offset-geometry framework where plumb-line curvature equals the surface gradient of $\log g$ (classical), using the public 2017 Geoid Slope Validation Survey (GSVS17) as the worked example, we calibrate, combine, and verify such a rule from three computable ingredients. (i) Identifiability: a row-space map from geometry to the recoverable Hessian components: a single profile constrains two or three contractions, the horizontal block needs areal or crossing coverage, and areal DoV plus gravity gradients, with the exterior field equation, reach the full symmetric Hessian (its trace fixed by the field equation). (ii) Detectability: for the stated local-polynomial operators the curvature noise floor scales as $\sigma_\kappa \propto \sigma\sqrt{\Delta s}/\ell^p$ ($p = 5/2$ for GNSS/leveling heights, 3/2 for astrogeodetic deflections), so the smallest detectable feature is $A_{\min} \propto \sigma_N\sqrt{\Delta s/\lambda}$, and the deflection channel detects features $\sim 15\times$ smaller (GSVS17/CODIAC budget). (iii) Confound control: the terrain plumb-line-curvature signal (an a-priori fixed-density prism reproduces it, correlation 0.75) is removable once the DEM resolves the terrain surviving the smoothing, giving a critical resolution $d_{\mathrm{crit}} \simeq 30''$ in rugged relief. The rule reproduces GSVS17's curvature noise floor from its design alone; with the measured signal this is an SNR of ≈ 1.8, showing that at 1.5 km spacing and ~ 10 mm per-mark height precision it validates curvature only near the centimetre scale, at the GEOID18 hybrid-model fit level, so the test sharpens with denser spacing, astrogeodetic deflections, or both.

Keywords: physical geodesy; geoid validation; deflection of the vertical; plumb-line curvature; gravity Hessian; identifiability; GSVS17

1 Introduction

Geoid-model validation campaigns compare independently observed geoid heights and geoid *slopes* against gravimetric or hybrid models. The Geoid Slope Validation Surveys (GSVS) of the U.S. National Geodetic Survey (Smith et al., 2013; Wang et al., 2017; van Westrum et al., 2021) compare GNSS/leveling-derived geoid heights $N = h - H$ and astrogeodetic deflections of the vertical against model predictions. Writing N for the geoid undulation, s for along-profile arc length, θ_A for the directional deflection, and a subscript for the differential order, the validation hierarchy is

$$N \;\longrightarrow\; \frac{\mathrm{d}N}{\mathrm{d}s} \approx -\theta_A \;\longrightarrow\; \frac{\mathrm{d}^2N}{\mathrm{d}s^2} \approx -\frac{\mathrm{d}\theta_A}{\mathrm{d}s}. \tag{1}$$

Height residuals test vertical separation, slope residuals the first derivative, and *curvature-level* residuals the local change of slope. This paper asks, with real data, how much a curvature-level residual adds and what limits it.

The motivating geometry is classical. Orthometric height is reckoned along the curved plumb line, and the curvature of the plumb line (the change of the gravity direction with height) has long been studied in astronomical and gravimetric geodesy (Groten, 1981; Heiskanen and Moritz, 1967; Jekeli, 2000), reaching several arc-seconds in rugged terrain (Groten, 1981). We do not claim plumb-line curvature as new. Our contributions are: (i) a computable row-space (identifiability) map that recasts the classical gravity-gradient↔deflection relations (Jekeli, 1999; Völgyesi, 2005; Jekeli, 2019) and the degrees-of-freedom content of gravimetric inverse theory and gradiometry (Rummel et al., 2011) as a survey-design diagnostic; (ii) a propagated detectability analysis of the curvature residual on GSVS17; and (iii) a real-data demonstration that the disagreement between the two GSVS curvature channels is dominated by a terrain-driven plumb-line-curvature signal, and that an a-priori prism terrain reduction (Nagy, 1966; Nagy et al., 2000; Forsberg, 1984) partially removes it. The resulting design rule (Section 6) is the validation-side complement of the geoid data-requirements and omission-error analyses that relate model resolution to the height-anomaly power spectrum (Jekeli, 2012; Foroughi et al., 2023): where those prescribe the data needed to *determine* a centimetre geoid, we quantify the survey needed to *detect* a geoid error at the curvature level. The scope is deliberately conservative: standard ellipsoidal geometry and reference-surface metrics already account for the intended reference geometry (Moritz, 1980; Karney, 2013; Torge and Müller, 2012), and the ellipsoid normal serves as the zero-curvature control case (the Appendix).

2 Background: the plumb line and its curvature

Let W be a C^3 gravity potential on a region with $\nabla W \neq 0$, with equipotential surfaces $\Sigma_c = \{W = c\}$, gravity vector $\boldsymbol{g} = \nabla W$, magnitude $g = \|\boldsymbol{g}\|$, and unit direction $\boldsymbol{u} = \boldsymbol{g}/g$ (Hofmann-Wellenhof and Moritz, 2005). The plumb line is the integral curve of $\boldsymbol{u}$. Differentiating $\boldsymbol{u} = g^{-1}\nabla W$ along $\boldsymbol{u}$ gives the curvature vector of the plumb line,

$$\nabla_{\boldsymbol{u}}\boldsymbol{u} = \frac{(I - \boldsymbol{u}\otimes\boldsymbol{u})\,(\nabla^2 W)\,\boldsymbol{u}}{g} = \nabla_\Sigma \log g, \tag{2}$$

the tangential projection of the gravity Hessian acting on $\boldsymbol{u}$, equivalently the surface gradient of $\log g$ (Jekeli, 2000; Groten, 1981). This intrinsic-geometry description of the field through the curvatures of the plumb line and the equipotential surfaces is classical (Hotine, 1969; Marussi, 1985). Every quantity below is a projection or contraction of $\nabla^2 W$, and Eq. (2) is the mechanism behind the confound in Section 5. The corresponding control statement, that a fixed-footpoint ellipsoid-normal height line is straight in Earth-centred coordinates so that ordinary ellipsoidal height carries no analogous curvature and the metric factors $(M + h), (\nu + h)$ are recovered exactly (with M, ν the meridional and prime-vertical radii), is elementary and is deferred to the Appendix.

3 Curvature-level residuals and their estimation

For a profile with unit horizontal tangent $\boldsymbol{t}_A = \cos A\,\boldsymbol{e}_N + \sin A\,\boldsymbol{e}_E$ at azimuth A, the directional deflection is $\theta_A = \xi\cos A + \eta\sin A$, with (ξ, η) the north/east DoV components, and the astrogeodetic leveling relation gives $\mathrm{d}N/\mathrm{d}s \approx -\theta_A$ (Hirt et al., 2010; Jekeli and Kwon, 2002; Albayrak et al., 2024). We define two profile residuals against a model (superscript m):

$$R_{N''}(s) := \tfrac{\mathrm{d}^2}{\mathrm{d}s^2}\left(N^{\mathrm{obs}} - N^{\mathrm{m}}\right), \qquad R_{\theta'}(s) := \tfrac{\mathrm{d}}{\mathrm{d}s}\left(\theta_A^{\mathrm{obs}} - \theta_A^{\mathrm{m}}\right). \tag{3}$$

By Eq. (1), $R_{N''}$ from leveling/GNSS and $-R_{\theta'}$ from observed DoV are, after the surface deflections are reduced to the geoid (equivalently, after accounting for the plumb-line-curvature term isolated in Section 5.3), two *independent* estimates of the same geoid-error curvature; their agreement is the central test. We estimate derivatives with Gaussian-weighted local cubic regression of bandwidth ℓ (Fan and Gijbels, 1996), which yields value, first, and second derivatives as exact linear operators L_0, L_1, L_2, so that input covariances propagate exactly, $C_{R_{N''}} = L_2 C_N L_2^\top$ and $C_{R_{\theta'}} = L_1 C_\theta L_1^\top$. The smoothing scale ℓ is part of the observable definition and we report results as a function of ℓ; scales $\ell \lesssim 1\,\mathrm{km}$ lie below the 1.6 km station spacing and are shown only to bound behaviour. Because L_2 annihilates any affine function of s, $R_{N''}$ is exactly insensitive to a constant frame/datum offset and to any linear tilt (numerically identical to one part in 10^8 here), so the large mean GSVS17−GEOID18 offset is irrelevant to the curvature observable.

4 Identifiability of projected equipotential geometry

In a local east–north–up frame with vertical $\boldsymbol{u}$, the symmetric Hessian $\nabla^2 W$ has six components $\boldsymbol{p} = (W_{ee}, W_{nn}, W_{uu}, W_{en}, W_{eu}, W_{nu})$, and each observable is a linear functional of $\boldsymbol{p}$:

- DoV profile at azimuth A: $\mathrm{d}\xi/\mathrm{d}s \propto W_{nn}\cos A + W_{en}\sin A$ and $\mathrm{d}\eta/\mathrm{d}s \propto W_{en}\cos A + W_{ee}\sin A$ (the north and east components of the along-profile derivative of the tangential vertical, i.e. the tangential shape operator);
- gravity-magnitude gradient: $\mathrm{d}\log g/\mathrm{d}s \propto W_{nu}\cos A + W_{eu}\sin A$ (Eq. 2);
- free-air field equation $W_{ee} + W_{nn} + W_{uu} = 2\omega^2$ (the exterior relation; inside topographic mass a Poisson density term enters);
- full-tensor gradiometry: all six components.

The kind of statement that follows must be stated carefully. A single observation at one point and azimuth supplies the listed contractions *at that point*; assembling several azimuths into a design matrix G presumes they probe the *same* Hessian. We therefore read identifiability as a survey-*design* row-space diagnostic, under the idealization that $\nabla^2 W$ is constant over the window within which the azimuth varies (equivalently, $\boldsymbol{p}$ as coefficients of a prescribed local model). This characterizes which combinations a given observation set *can* constrain; it is not a claim that a single, spatially varying profile recovers the local Hessian pointwise. Genuine pointwise recovery of the horizontal block requires azimuth diversity *at* a point, that is, areal or crossing geometry. Under this reading, identifiability follows from rank(G), the null space, and the conditioning (Table 1, Fig. 1).

Proposition 1 (Row space by geometry, under local constancy) *(a) A single straight DoV profile spans a rank-2 row space: two contractions of the horizontal block $\{W_{ee}, W_{nn}, W_{en}\}$, which two depending on azimuth (a near east–west line constrains W_{ee} and W_{en} but barely W_{nn}). Adding the gravity gradient gives rank 3. (b) The GSVS17 corridor azimuth set (DoV plus gravity gradient, $\sim 24°$–$146°$ (5–95th percentile, s.d. 37°; the corridor winds through terrain)) spans a rank-5 row space, all but W_{uu}, at condition number ≈ 2; this is a design upper bound under local constancy, not pointwise recovery from the real field. (c) The field equation adds W_{uu} (rank 6). (d) Areal DoV spans the horizontal block (rank 3); areal DoV plus the areal gravity gradient adds $\{W_{eu}, W_{nu}\}$ (rank 5); with the trace it reaches rank 6, the same components as full-tensor gradiometry up to conditioning.*

Because the resolution diagonal is basis-dependent, the invariant content is the rank and the null space. For a near east–west single DoV+gravity profile the null space is dominated by W_{nn},

Table 1: Row-space rank, condition number κ (of the nonzero singular spectrum), and resolution diagonal $\mathrm{diag}(R)$ per Hessian component by survey geometry (under local constancy; 1 constrained, 0 null). The diagonal is basis-dependent and is shown for orientation only; rank and the null space (text) are the invariant statements. Here g in the geometry labels denotes the along-profile gravity-magnitude gradient $\mathrm{d}\log g/\mathrm{d}s$ (Eq. 2), not scalar gravity.

geometry	rank	κ	W_{ee}	W_{nn}	W_{uu}	W_{en}	W_{eu}	W_{nu}
1 straight profile, DoV	2	1.1	1.00	0.02	0.00	0.99	0.00	0.00
1 straight profile, DoV+g	3	1.1	1.00	0.02	0.00	0.99	0.99	0.01
GSVS17 azimuth set, DoV+g	5	1.9	1.00	1.00	0.00	1.00	1.00	1.00
areal DoV	3	1.4	1.00	1.00	0.00	1.00	0.00	0.00
areal DoV + areal g	5	1.4	1.00	1.00	0.00	1.00	1.00	1.00
areal DoV +g+ field eq.	6	5.3	1.00	1.00	1.00	1.00	1.00	1.00
full-tensor gradiometry	6	1.0	1.00	1.00	1.00	1.00	1.00	1.00

W_{uu}, and the cross-vertical component orthogonal to the along-profile gravity-gradient contraction, consistent with Proposition 1(a).

Corollary 1 (Survey design) *Identifiability is governed by azimuth diversity at a point, not station count: a single-azimuth corridor, however dense, cannot separate the horizontal block, whereas crossing lines or an areal pattern give well-conditioned local recovery.*

Proposition 1 reframes the confound of Section 5: the surface-DoV channel is not failing but sensing a projection of $\nabla^2 W$ that profile-only data cannot fully separate pointwise. The observables differ in kind: the scalar curvature residual of Section 3 uses one directional contraction θ_A, while the row-space map retains both DoV components (ξ, η), which is what supplies two horizontal-block contractions along a single line (CODIAC measures both).

5 GSVS17 demonstration

We use the public GSVS17 field data (van Westrum et al., 2021; National Geodetic Survey, 2021): 222 stations from Durango to Walsenburg, Colorado, over a 340.7 km horizontal-geodesic line at ≈ 1.54 km spacing. The survey provides GNSS ellipsoidal heights h, first-order leveling orthometric heights H, absolute gravity, vertical gravity gradients, CODIAC astrogeodetic surface deflections (ξ, η), and airborne gravity over the line. We use h, H and DoV for the curvature-residual demonstrations; absolute gravity enters only the survey-design discussion (Section 4). The vertical gravity gradients and airborne data are not used in the present analysis. GEOID18 and USGG2012 model values were obtained at every station from the NGS Geoid Height Service (National Geodetic Survey, 2026). Throughout, the model deflection is the GEOID18 geoid-surface slope ($-\mathrm{d}N^{\mathrm{GEOID18}}/\mathrm{d}s$), not DEFLEC18, which represents surface deflections and so already includes the plumb-line-curvature term (Section 5.3). Along-profile distance is the horizontal geodesic, matching the survey's geodesic intervals to 0.3 m; the spreadsheet "distance from Durango" is the leveling/road distance and is not the correct coordinate for $\mathrm{d}N/\mathrm{d}s = -\theta_A$.

5.1 Observed two-channel curvature

After removing a best-fitting linear trend (which leaves $R_{N''}$ unchanged), the detrended height residual against GEOID18 has RMS 35.3 mm and the raw offset is -0.94 m, reproducing the published GSVS17 figures (35.7 mm, -0.93 m) and confirming the implementation. At the slope level

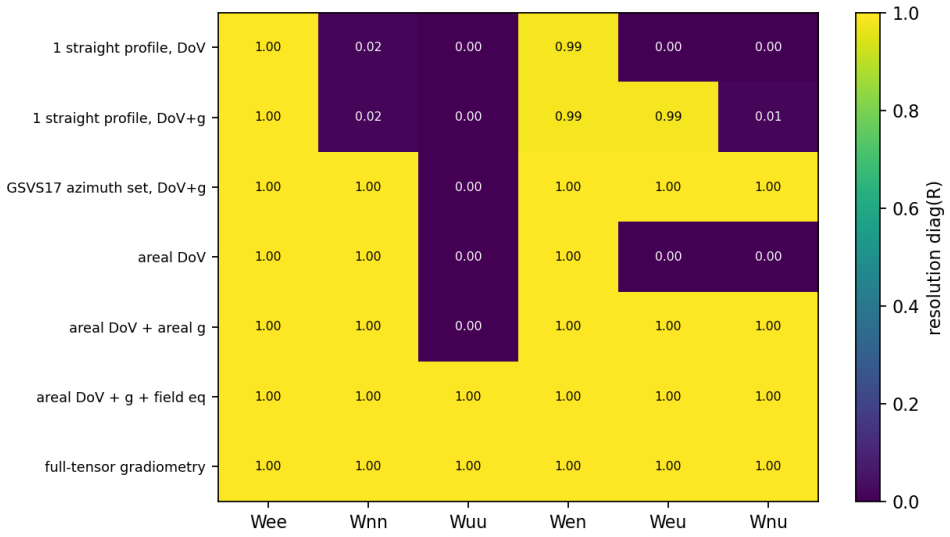

Figure 1: Row-space resolution diagonal by survey geometry, under local constancy. The GSVS17 azimuth set spans five of six components; only W_{uu} requires the field equation, and areal DoV plus gravity gradients span the full gradiometric set, with the field equation. Diagonal values are basis-dependent (see text).

the two observation systems agree well, $\mathrm{corr}(\mathrm{d}N/\mathrm{d}s, -\theta_A) = +0.945$, RMS misfit $2.06''$. Computing the geoid *curvature* two ways, $\mathrm{d}^2N/\mathrm{d}s^2$ from leveling/GNSS and $-\mathrm{d}\theta_A/\mathrm{d}s$ from CODIAC, the two independent channels agree strongly on the *raw* geoid curvature (correlation +0.90, stable over $\ell = 1$–$10\,\mathrm{km}$): the curvature observable is computable from real, fully independent data and the channels cross-validate.

5.2 Detectability and the error budget

We propagate the GSVS17 budget using the published accuracies, geoid undulation $\approx 1.5\,\mathrm{cm}$ between marks and surface deflections $0.04''$ (van Westrum et al., 2021), plus a data-derived orthometric-height term from the two leveling reductions in the file (standard vs. Remmer refraction; RMS 10.7 mm, contributing $0.11\,\mathrm{mm\,km^{-2}}$ at the curvature level). The curvature residual against GEOID18 is $1.84\,\mathrm{mm\,km^{-2}}$ at $\ell = 2\,\mathrm{km}$, only an SNR of ~ 1.8 above the height-channel floor, reaching ≈ 3 near $\ell = 3\,\mathrm{km}$ (Table 2, Fig. 2). Because the DoV floor at $0.04''$ is far smaller ($\sim 0.06\,\mathrm{mm\,km^{-2}}$), the curvature observable is effectively a *deflection* instrument; the GNSS/leveling height channel is noise-limited and cannot independently confirm it except at long wavelengths.

The floor in Table 2 propagates observation noise only and is therefore a lower bound: model interpolation and grid-resolution error, correlated GNSS/leveling errors along the route, DoV systematics, and the smoothing-bandwidth choice all add variance that would *raise* the floor and lower the SNR, reinforcing the detectability-limited conclusion. NGS also notes that the GEOID18 "estimated uncertainty" reflects the fit to NAVD88 bench marks rather than absolute geoid accuracy (Ahlgren et al., 2020), so we do not treat the model as error-free. The model-to-model curvature background (GEOID18−USGG2012) is $\approx 0.5\,\mathrm{mm\,km^{-2}}$ at $\ell = 2$; the observed residual exceeds it by $\sim 3\times$, falling to $\sim 2\times$ at heavier smoothing, never by the order of magnitude obtained when numerator and denominator are evaluated at different scales. Because GEOID18 is a hybrid

Table 2: Curvature-residual RMS, height-channel observation-noise floor, and signal-to-noise ratio (SNR = RMS residual / 1σ floor; an SNR, not a formal p-value) vs. smoothing scale ℓ (interior stations; $\ell \lesssim 1$ km is below station spacing).

ℓ (km)	1.0	1.5	2.0	3.0	5.0	7.0	10.0
$R_{N''}$ RMS (mm km^{-2})	4.70	2.62	1.84	1.15	0.61	0.32	0.14
floor 1σ	6.44	2.15	1.03	0.39	0.12	0.063	0.035
SNR ($R_{N''}/\sigma_{\mathrm{fl}}$)	0.7	1.2	1.8	3.0	5.0	5.0	3.9

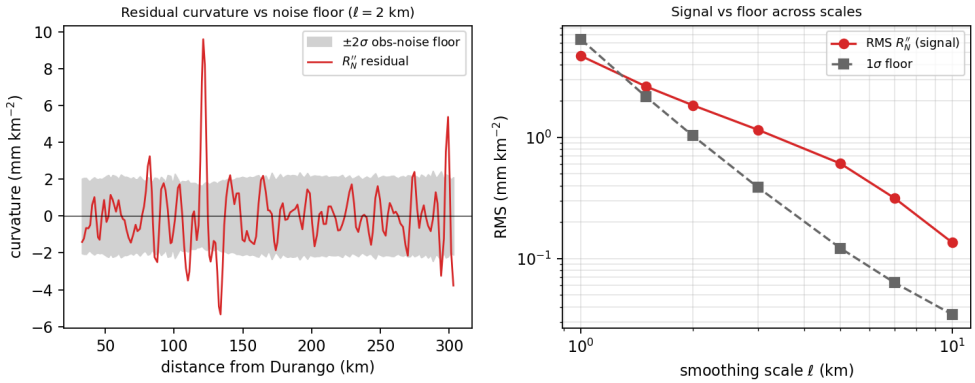

Figure 2: Left: residual curvature against the $\pm 2\sigma$ propagated observation-noise floor at $\ell = 2$ km. Right: RMS curvature signal and the 1σ floor across smoothing scales (cf. Table 2); the residual is marginal (SNR ≈ 1.8) at $\ell = 2$ km and crosses SNR$= 3$ near $\ell = 3$ km.

NAD83/NAVD88 surface whereas USGG2012 is gravimetric in IGS08/GRS80 (National Geodetic Survey, 2012), curvature removes constant offsets and linear tilts but not the local curvature of the hybrid conversion surface, so this background is a conservative, not exhaustive, proxy for model uncertainty. We therefore report the SNR against a propagated noise floor rather than a bare ratio.

5.3 The plumb-line-curvature confound and an a-priori terrain reduction

Against a model the two curvature channels agree only weakly (correlation +0.25 at $\ell = 2$ km). By Eq. (1) their difference is $R_{N''} + R_{\theta'} = \mathrm{d}(\theta_{\mathrm{surf}} - \theta_{\mathrm{geoid}})/\mathrm{d}s$, the derivative of the surface-to-geoid deflection difference $\delta\theta$ (RMS $2.06''$, the magnitude expected for plumb-line curvature in rugged terrain). It is essential to state the model-deflection convention. Here the model slope is the GEOID18 *geoid-surface* slope, equivalently $-\mathrm{d}N^{\mathrm{GEOID18}}/\mathrm{d}s$; we do *not* use the DEFLEC18 surface-deflection model, which represents deflections at the Earth's surface and so already includes the plumb-line-curvature term (Ahlgren et al., 2020). Hence $\delta\theta$ is the raw surface-to-geoid plumb-line curvature; differencing against DEFLEC18 would instead yield a residual of the modeled correction.

We test the terrain origin with an *a-priori* forward model: the closed-form gravitational attraction of right rectangular prisms (Nagy, 1966; Nagy et al., 2000) representing the $3''$ SRTM topography (Farr et al., 2007; OpenTopography, 2013) from the geoid ($h = 0$) to the surface, evaluated at each station, with fixed crustal density 2670 kg m^{-3}, a near zone of $\pm 0.13°$, the stable logarithm form for near-nadir cells, and *no fitted scale*. The amplitude and density are fixed a priori, and the sign follows from the slope-level deflection convention $\mathrm{d}N/\mathrm{d}s = -\theta_A$, fixed before the curvature correlation is examined (both signs, ± 0.75, are reported as a sanity check). The

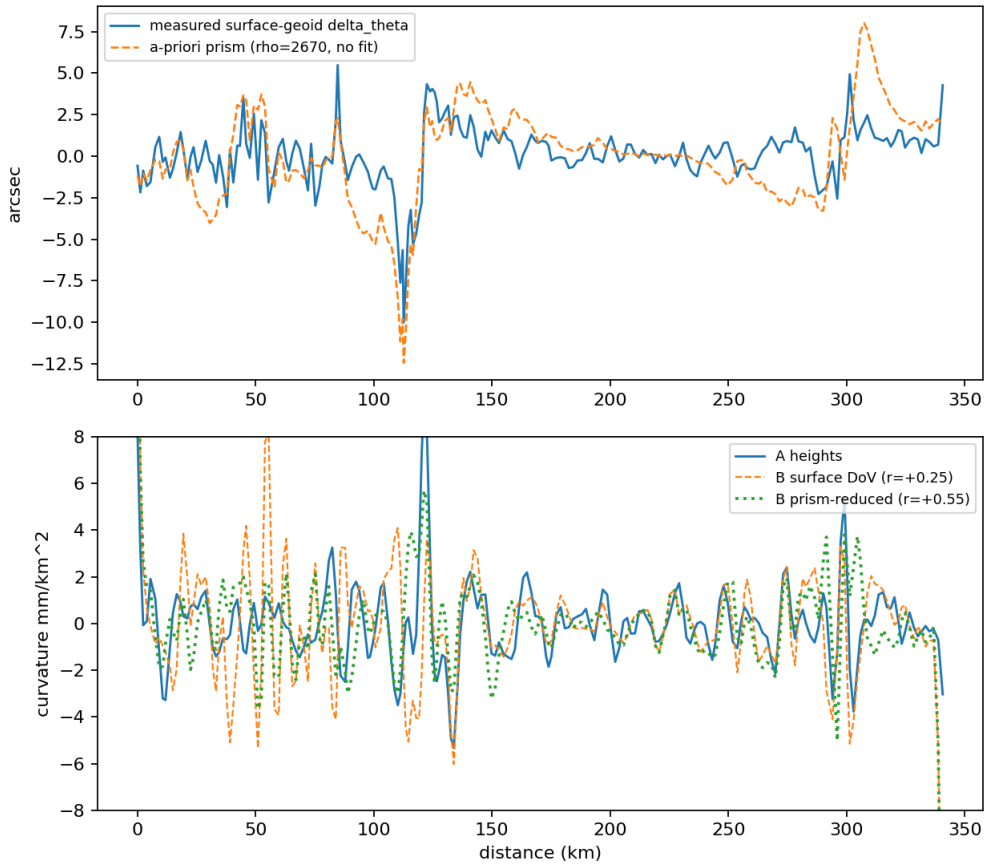

Figure 3: Top: the measured surface−geoid deflection difference and its a-priori rectangular-prism prediction (fixed density, no fitted amplitude scale; $r = 0.75$). Bottom: the two curvature channels before and after the unfitted terrain reduction of the surface DoV; the reduced DoV channel tracks the height channel substantially better (correlation $0.25 \rightarrow 0.55$).

model reproduces $\delta\theta$ in shape (correlation 0.75) and order of magnitude ($2.9''$ predicted vs. $2.06''$ observed). Subtracting the unfitted prediction raises the two-channel curvature correlation from 0.25 to 0.55 and cuts the disagreement from 2.50 to $1.68\,\mathrm{mm\,km^{-2}}$ (Fig. 3). The correlation is robust to DEM resolution (0.75 at both $3''$ and $9''$), indicating the effect is driven by terrain at scales the $3''$ data already resolve. The amplitude factor ($\sim 1.4\times$) is consistent with long-wavelength terrain already captured by GEOID18. The agreement is not an artifact of these choices. Against phase-randomized surrogates that preserve each channel's power spectrum, the prism correlation $r = 0.75$ lies about 4σ above the null ($p < 0.001$; the raw two-channel correlation 0.90 is 6σ). It is also stable to the free parameters: 0.72 to 0.82 across the interior fraction, 0.61 to 0.85 as the near-zone radius runs from 29 down to 7 km (the reported value uses the conservative 14 km), and invariant to the smoothing scale and to a $\pm 10\%$ density change. A $1''$/LiDAR DEM would further refine the near field. The terrain origin of the confound is thus well supported, with no fitted scale.

6 A design rule for curvature-level validation

Sections 4–5.3 isolate the three quantities that govern a curvature-level test: identifiability (which Hessian components the geometry constrains), detectability (signal against the propagated noise floor), and the terrain confound. We now combine them into a predictive rule – given a survey design, is a curvature-level comparison warranted, and at what feature size does it become decisive?

Detectability law. The curvature estimator is a fixed linear operator (L_2 for the height channel; L_1 applied to the deflections for the astrogeodetic channel; Section 3). For the Gaussian-weighted local-cubic operators on a profile of uniform spacing Δs smoothed at scale ℓ, the interior curvature noise floor (1σ, RMS) is, to within a constant calibrated exactly from the operators,

$$\sigma_\kappa^{\text{height}} = c_h\,\sigma_N\,\frac{\sqrt{\Delta s}}{\ell^{5/2}}, \qquad \sigma_\kappa^{\text{DoV}} = c_d\,\sigma_\theta\,\frac{\sqrt{\Delta s}}{\ell^{3/2}}, \tag{4}$$

with $c_h = 0.460$ and $c_d = 0.696$ (dimensionless, SI; the fitted exponents are -2.499 and -1.499 in ℓ and $+0.500$ in Δs, and the constants are stable to $< 10^{-4}$ across all $\Delta s, \ell$). The $\ell^{-(2m+1)/2}$ scaling of an mth-derivative estimator is the standard local-polynomial variance law (Fan and Gijbels, 1996); the contribution here is its calibration for the geodetic operators and its synthesis with identifiability and the terrain confound into a single design rule. A geoid feature of height amplitude A and wavelength λ presents curvature amplitude $(2\pi/\lambda)^2 A$; Gaussian smoothing attenuates the curvature (L_2) channel by exactly $\exp(-2\pi^2\ell^2/\lambda^2)$ (verified numerically to unity at the reported precision), maximised at $\ell_{\text{opt}} \simeq \lambda/4$. The minimum detectable feature amplitude (peak smoothed curvature $= 3\sigma_\kappa$) then has the closed form, for the height channel,

$$A_{\min} = 8.34\,c_h\,\sigma_N\sqrt{\Delta s/\lambda} \;\propto\; \sigma_N\sqrt{\Delta s/\lambda}, \tag{5}$$

so detectability improves with height precision, denser spacing, and longer wavelength. The deflection channel's first-derivative attenuation is not Gaussian (it passes more signal), so its $A_{\min}$ is evaluated directly from L_1.

Anchoring on GSVS17. At the GSVS17 geometry ($\Delta s = 1.54\,\text{km}$, $\sigma_N = 10\,\text{mm}$), Eq. (4) reproduces the curvature floor obtained from the full covariance propagation on the real 222-station line: 1.010 vs. 1.012 mm km^{-2} at $\ell = 2\,\text{km}$ and 0.366 vs. 0.367 at $\ell = 3\,\text{km}$ (the small gap to Table 2 is the leveling random-walk and refraction terms). With the measured signal of 1.84 mm km^{-2} this is an SNR of ≈ 1.8: the marginal detectability of Section 5.2 is exactly what the rule predicts from the design alone, so Eq. (5) is appropriate for first-order design extrapolation. Here σ_N is the white-noise-equivalent per-mark geoid-height uncertainty entering L_2; we take $\sigma_N = 10\,\text{mm}$ for GSVS17 (the $\sim 1.5\,\text{cm}$ between-mark agreement is $\sqrt{2}$ times this). Because the height-channel floor scales linearly with σ_N, the SNR scales inversely; a more conservative 13 or 15 mm lowers the $\ell = 2\,\text{km}$ value to SNR ≈ 1.4 or 1.2.

What the rule requires. Table 3 and Fig. 4(a) give $A_{\min}$ over realistic spacings and precisions. At GSVS17's design the height channel resolves curvature features only down to $A_{\min} \simeq 11\,\text{mm}$ at $\lambda = 20\,\text{km}$ – the same order as GEOID18's stated $\sim 15\,\text{mm}$ hybrid-model uncertainty, which is why the residual is marginal. Reaching the centimetre and below requires roughly twice-denser spacing, twice-better σ_N, or the deflection channel: astrogeodetic deflections at $0.04''$ detect features about $15\times$ smaller ($A_{\min} \simeq 0.7\,\text{mm}$ at GSVS17 spacing; Fig. 4(b)), so for curvature work the GNSS/leveling height precision, not the deflection precision, is the binding constraint.

Table 3: Minimum detectable geoid-height feature amplitude $A_{\min}$ (mm) at SNR= 3, $\lambda = 20\,\mathrm{km}$, from Eqs. (4)–(5): height channel at three GNSS/leveling precisions and the deflection channel at CODIAC 0.04″. GSVS17's design is in bold.

	height channel, σ_N			deflection
spacing Δs	5 mm	10 mm	15 mm	0.04″
0.50 km	3.0	6.1	9.1	0.40
1.00 km	4.3	8.6	12.9	0.56
1.54 km	5.3	**10.7**	16.0	**0.70**
3.00 km	7.4	14.9	22.3	0.98

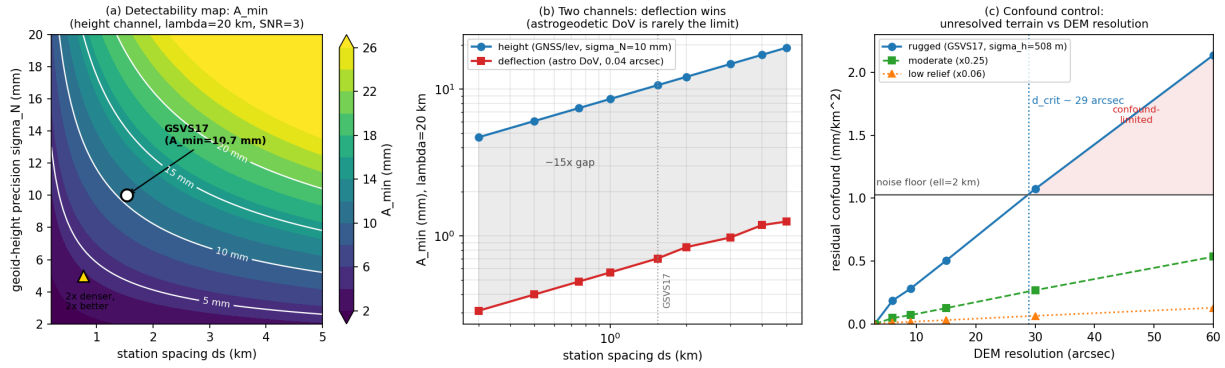

Figure 4: Design rule. (a) Minimum detectable feature amplitude $A_{\min}$ (height channel, $\lambda = 20\,\mathrm{km}$, SNR= 3) over station spacing and geoid-height precision, with GSVS17 marked. (b) The deflection channel detects features $\sim 15\times$ smaller than GNSS/leveling at the same spacing, so it is rarely the binding constraint. (c) Residual (unresolved) terrain-curvature confound vs. DEM resolution; a DEM is adequate where this falls below the noise floor ($d_{\mathrm{crit}} \simeq 30''$ for rugged terrain, relaxing with relief).

Terrain requirement. The confound is removable to the extent the DEM resolves the terrain that survives the smoothing. Degrading the a-priori prism model (Section 5.3), the residual unresolved confound grows from $0.19\,\mathrm{mm\,km^{-2}}$ at 6″ to 1.07 at 30″ and 2.14 at 60″ (Fig. 4(c)); set against the $\sim 1\,\mathrm{mm\,km^{-2}}$ floor, the criterion "residual < floor" gives a critical resolution $d_{\mathrm{crit}} \simeq 30''$ for rugged terrain ($\sigma_h = 508\,\mathrm{m}$ here). Thus 3″ terrain is unnecessary and 9–15″ is ample – which is why the 3″ and 9″ reductions agree (Section 5.3): at kilometre smoothing only medium-wavelength terrain reaches the curvature channel. Because the confound scales with relief, in moderate or low terrain the requirement relaxes further.

Across the spectrum. A single feature wavelength is a simplification; real model errors occupy a band. Figure 5 compares $A_{\min}(\lambda)$ (height channel, GSVS17 design) with the along-profile amplitude spectrum of the GEOID18−USGG2012 difference, a proxy for model-level discrepancy. The two cross near 50–60 km: GSVS17 validates curvature only for the long-wavelength ($\sim$ 60–110 km), large-amplitude part of the discrepancy, while shorter scales fall below the floor. Because $A_{\min} \propto \lambda^{-1/2}$ while a power-law geoid spectrum rises toward long wavelengths, this band is set by the intersection of the survey floor with the height-anomaly spectrum (Jekeli, 2012; Foroughi et al., 2023) – the curvature-validation analogue of the omission-error and data-requirements relations

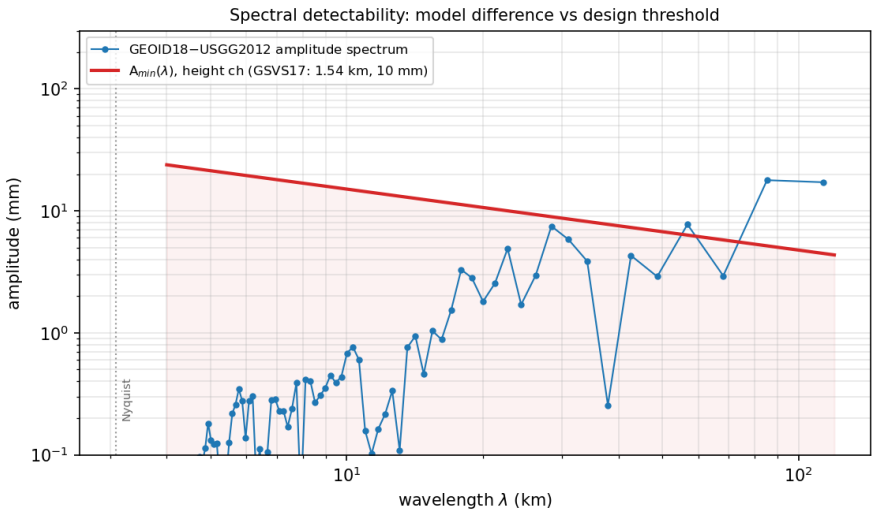

Figure 5: Spectral detectability. The design threshold $A_{\min}(\lambda)$ (height channel, GSVS17 design) against the along-profile amplitude spectrum of the GEOID18−USGG2012 difference. Only where the spectrum exceeds $A_{\min}$ (here ∼60–110 km wavelength) can the survey validate the discrepancy at the curvature level. The spectrum is the one-sided, Hann-tapered (amplitude-corrected) amplitude per Fourier component of the linearly detrended difference resampled to uniform spacing; the Nyquist wavelength is $2\Delta s \approx 3$ km.

used in geoid *determination*.

7 Discussion

The design rule (Section 6) recasts the GSVS17 findings as a feasibility statement; here we place them in the validation literature. GSVS17 supports three uses. The two independent channels cross-validate the raw geoid curvature (correlation 0.90). The astrogeodetic channel, at 0.04″, is a precise curvature sensor: its noise floor lies an order of magnitude below the GNSS/leveling channel. And the row-space map (Section 4) states which projected-Hessian components a given survey design can constrain; areal DoV plus gravity gradients, with the exterior field equation, reach the gradiometric set (Rummel et al., 2011). The residuals extend GSVS logic (Smith et al., 2013; Wang et al., 2017; van Westrum et al., 2021; Wang et al., 2021) by one differential order. The limits are concrete. The model residual is only an SNR of ∼1.8 above the propagated floor at $\ell = 2$ km, clearing ≈ 3 near 3 km, and it exceeds the model background by only ∼3×. The channel difference is dominated by the plumb-line-curvature signal: terrain-driven ($r = 0.75$, a-priori prism model) and only partially removable without high-resolution terrain or dense gravity. This is consistent with the limited row space of a single profile (Proposition 1): the plumb-line-curvature term loads on the cross-vertical Hessian components W_{eu}, W_{nu}, which profile-only data do not fully isolate. Curvature-level residuals are best used as a diagnostic in a declared wavelength band, reporting the smoothing scale, the propagated covariance, the surface/geoid deflection convention, and an explicit terrain/gravity reduction, with crossing or areal geometry (Corollary 1) where the full projected geometry is wanted.

8 Conclusions

Curvature-level geoid validation is governed by three computable quantities (Section 6): which components of the gravity Hessian the survey geometry constrains, a detectability floor $\sigma_\kappa \propto \sigma\sqrt{\Delta s}/\ell^p$ that fixes the smallest validatable feature amplitude $A_{\min} \propto \sigma_N\sqrt{\Delta s/\lambda}$, and a terrain criterion $d_{\mathrm{crit}} \simeq 30''$ in rugged relief for the plumb-line-curvature confound. Evaluated at the GSVS17 design alone, the rule reproduces the curvature noise floor, which with the measured signal gives an SNR of ≈ 1.8. Underlying all of it is one classical fact: plumb-line curvature is the surface gradient of $\log g$, so every curvature-level observable here is a projection or contraction of the gravity Hessian.

As a survey-design diagnostic, a single profile constrains only two or three Hessian contractions, and recovering the horizontal block requires areal or crossing coverage; areal deflections together with gravity gradients and the field equation reach the full symmetric Hessian, its sixth component fixed by the trace. What sets this is the spread of azimuths at a point, not the number of stations. On GSVS17 the curvature residual against GEOID18 is computable but marginal (Section 5.2), exceeding the model background by roughly $3\times$ rather than the order of magnitude a mismatched comparison would suggest. The astrogeodetic channel, needing one fewer derivative, detects features about $15\times$ smaller.

Curvature-level validation is therefore feasible and quantifiable, and it becomes decisive once spacing, height precision, or astrogeodetic deflections carry a survey across the $A_{\min}$ and d_{crit} thresholds. At GSVS17's spacing and precision it sits at the centimetre margin.

Appendix: the ellipsoid normal carries no curvature

Fix geodetic latitude ϕ and longitude λ and vary only ellipsoidal height h in the Earth-centred coordinates $X = (\nu + h)\cos\phi\cos\lambda$, $Y = (\nu + h)\cos\phi\sin\lambda$, $Z = (\nu(1 - e^2) + h)\sin\phi$, where ν is the prime-vertical radius of curvature. Then $\partial^2\boldsymbol{x}/\partial h^2 = \mathbf{0}$, so the height line is straight and has zero Euclidean curvature, and integrating the first-order shell transport recovers the metric factors $(M+h), (\nu+h)$ exactly (with M the meridional radius). Any nonzero plumb-line curvature therefore arises from the physical equipotential family, not from ordinary ellipsoidal offsets: the zero-curvature control against which the results of Section 2 are stated.

Acknowledgements. We thank the U.S. National Geodetic Survey for the publicly available GSVS17 field data and geoid models, and OpenTopography for the SRTM digital elevation model.

Author contributions. R.D.M. conceived the study, performed the analysis, and wrote the manuscript.

Data and code availability. GSVS17 field data (van Westrum et al., 2021; National Geodetic Survey, 2021), GEOID18/USGG2012 model values (NGS geoid service), and the SRTM DEM (OpenTopography) are public. The processing scripts (identifiability, error budget, terrain reduction, and design rule) and derived station tables/figures are archived at Zenodo.

Funding. None declared.

Competing interests. The author declares no competing interests.

References

Ahlgren K, Scott G, Zilkoski D, Shaw B, Paudel N (2020) GEOID18. NOAA Technical Report NOS NGS 72, National Geodetic Survey, Silver Spring, MD. https://doi.org/10.25923/pc79-0q29

Albayrak M, Marti U, Willi D, Guillaume S, Hardy RA (2024) Precise geoid determination in the eastern Swiss Alps using geodetic astronomy and GNSS/leveling. Sensors 24(21):7072. https://doi.org/10.3390/s24217072

Fan J, Gijbels I (1996) Local Polynomial Modelling and Its Applications. Chapman & Hall, London.

Farr TG, Rosen PA, Caro E, et al. (2007) The Shuttle Radar Topography Mission. Rev Geophys 45:RG2004. https://doi.org/10.1029/2005RG000183

Foroughi I, Goli M, Pagiatakis S, Fergusson S, Novák P (2023) Data requirements for the determination of a sub-centimetre geoid. Earth-Sci Rev 239:104326. https://doi.org/10.1016/j.earscirev.2023.104326

Forsberg R (1984) A study of terrain reductions, density anomalies and geophysical inversion methods in gravity field modelling. OSU Report 355, Ohio State Univ.

Groten E (1981) Determination of plumb line curvature by astronomical and gravimetric methods. NOAA Tech. Memo. NOS NGS 30, National Geodetic Survey.

Heiskanen WA, Moritz H (1967) Physical Geodesy. Freeman, San Francisco.

Hirt C, Bürki B, Somieski A, Seeber G (2010) Modern determination of vertical deflections using digital zenith cameras. J Surveying Eng 136(1):1–12. https://doi.org/10.1061/(ASCE)SU.1943-5428.0000009

Hofmann-Wellenhof B, Moritz H (2005) Physical Geodesy. Springer, Vienna. https://doi.org/10.1007/978-3-211-33545-1

Hotine M (1969) Mathematical Geodesy. ESSA Monograph 2, U.S. Department of Commerce, Washington, DC.

Jekeli C (1999) An analysis of vertical deflections derived from high-degree spherical harmonic models. J Geod 73(1):10–22. https://doi.org/10.1007/s001900050213

Jekeli C (2000) Heights, the geopotential, and vertical datums. Report 459, Dept. of Civil and Environmental Eng. and Geodetic Science, Ohio State Univ.

Jekeli C (2012) Omission error, data requirements, and the fractal dimension of the geoid. In: VII Hotine-Marussi Symposium, IAG Symp 137:181–187. https://doi.org/10.1007/978-3-642-22078-4_27

Jekeli C (2019) Deflections of the vertical from full-tensor and single-instrument gravity gradiometry. J Geod 93(3):369–382. https://doi.org/10.1007/s00190-018-1162-y

Jekeli C, Kwon JH (2002) Geoid profile determination by direct integration of GPS/inertial navigation system vector gravimetry. J Geophys Res 107(B10):ETG3. https://doi.org/10.1029/2001JB001626

Karney CFF (2013) Algorithms for geodesics. J Geod 87(1):43–55. https://doi.org/10.1007/s00190-012-0578-z

Marussi A (1985) Intrinsic Geodesy. Springer, Berlin (translated by WI Reilly).

Moritz H (1980) Geodetic Reference System 1980. Bull Géod 54:395–405. https://doi.org/10.1007/BF02521480

Nagy D (1966) The gravitational attraction of a right rectangular prism. Geophysics 31(2):362–371. https://doi.org/10.1190/1.1439779

Nagy D, Papp G, Benedek J (2000) The gravitational potential and its derivatives for the prism. J Geod 74:552–560. https://doi.org/10.1007/s001900000116

National Geodetic Survey (2012) USGG2012 and GEOID12B technical details. https://geodesy.noaa.gov/GEOID/GEOID12B/ (accessed 2026).

National Geodetic Survey (2021) Geoid Slope Validation Survey 2017 (GSVS17): processed and raw field data. https://geodesy.noaa.gov/GEOID/GSVS17/ (accessed 2026).

National Geodetic Survey (2026) Geoid Height Service (API). https://geodesy.noaa.gov/web_services/geoid.shtml (accessed 2026).

OpenTopography (2013) Shuttle Radar Topography Mission Global 3 arc-second (SRTMGL3). https://doi.org/10.5069/G9445JDF.

Rummel R, Yi W, Stummer C (2011) GOCE gravitational gradiometry. J Geod 85(11):777–790. https://doi.org/10.1007/s00190-011-0500-0

Smith DA, Holmes SA, Li X, Guillaume S, Wang YM, Bürki B, Roman DR, Damiani TM (2013) Confirming regional 1 cm differential geoid accuracy from airborne gravimetry: the Geoid Slope Validation Survey of 2011. J Geod 87(10–12):885–907. https://doi.org/10.1007/s00190-013-0653-0

Torge W, Müller J (2012) Geodesy, 4th edn. De Gruyter. https://doi.org/10.1515/9783110250008

van Westrum D, Ahlgren K, Hirt C, Guillaume S (2021) A geoid slope validation survey (2017) in the rugged terrain of Colorado, USA. J Geod 95(1):9. https://doi.org/10.1007/s00190-020-01463-8

Völgyesi L (2005) Deflections of the vertical and geoid heights from gravity gradients. Acta Geod Geophys Hung 40(2):147–159. https://doi.org/10.1556/AGeod.40.2005.2.3

Wang YM, Becker C, Mader G, et al. (2017) The Geoid Slope Validation Survey 2014 and GRAV-D airborne gravity enhanced geoid comparison results in Iowa. J Geod 91:1261–1276. https://doi.org/10.1007/s00190-017-1022-1

Wang YM, Sanchez L, Agren J, et al. (2021) Colorado geoid computation experiment: overview and summary. J Geod 95:127. https://doi.org/10.1007/s00190-021-01567-9